

# Development of PARMA: PHITS-based Analytical Radiation Model in the Atmosphere

Tatsuhiko Sato,<sup>a,1</sup> Hiroshi Yasuda,<sup>b</sup> Koji Niita,<sup>c</sup> Akira Endo<sup>a</sup> and Lembit Sihver<sup>d</sup>

<sup>a</sup> Japan Atomic Energy Agency (JAEA); <sup>b</sup> National Institute of Radiological Sciences (NIRS); <sup>c</sup> Research Organization for Information Science and Technology (RIST); and <sup>d</sup> Chalmers University of Technology

---

Sato, T., Yasuda, H., Niita, K., Endo, A. and Sihver, L. Development of PARMA: PHITS-based Analytical Radiation Model in the Atmosphere. *Radiat. Res.* **170**, 244–259 (2008).

Estimation of cosmic-ray spectra in the atmosphere has been essential for the evaluation of aviation doses. We therefore calculated these spectra by performing Monte Carlo simulation of cosmic-ray propagation in the atmosphere using the PHITS code. The accuracy of the simulation was well verified by experimental data taken under various conditions, even near sea level. Based on a comprehensive analysis of the simulation results, we proposed an analytical model for estimating the cosmic-ray spectra of neutrons, protons, helium ions, muons, electrons, positrons and photons applicable to any location in the atmosphere at altitudes below 20 km. Our model, named PARMA, enables us to calculate the cosmic radiation doses rapidly with a precision equivalent to that of the Monte Carlo simulation, which requires much more computational time. With these properties, PARMA is capable of improving the accuracy and efficiency of the cosmic-ray exposure dose estimations not only for aircrews but also for the public on the ground. © 2008 by Radiation Research Society

---

## INTRODUCTION

At high altitude, aircrews are exposed to a high level of cosmic radiations. Protection for crew members against these terrestrial cosmic rays has been widely discussed since the publication of ICRP publication 60 (1), in which this aircrew exposure is recognized as an occupational hazard. As a result of this discussion, many countries have issued regulations (or recommendations) for an annual dose limitation for aircrews. Development of an aviation dose calculation code is indispensable for following the regulations, since the doses depend on the altitude, the geomagnetic location and the solar activity (referred to here as global conditions) along the flight routes in a complicated manner, and it is impractical to measure the doses for all flight conditions.

<sup>1</sup> Address for correspondence: Research Group for Radiation Protection, Division of Environment and Radiation Sciences, Nuclear Science and Engineering Directorate, Japan Atomic Energy Agency, Tokai, Naka, Ibaraki, 319-1195, Japan; e-mail: sato.tatsuhiko@jaea.go.jp.

Several calculation codes, e.g. EPCARD (2), CARI-6 (3) and PCAIRE (4), have been developed to estimate the aircrew dose. They can calculate route doses, the dose en route between two airports, by specifying the flight conditions, such as the departure and destination airports. The accuracy of the calculations was well verified by experimental data. However, the calculated dose is intrinsically derived from a non-physical quantity: the fluence-to-dose conversion coefficient, which depends significantly on its calculation model properties such as the dose type (the effective dose or the ambient dose equivalent), the radiation weighting factor, the characterization of the human model, and the irradiation geometry. Hence calculation results reflect the radiation protection policy adopted in the code. It is therefore worthwhile to develop a new route-dose calculation code that explicitly determines the atmospheric cosmic-ray spectra on flight routes and combines these data with user-specified fluence-to-dose conversion coefficients. Establishment of a reliable model for calculating the cosmic-ray spectra under any global conditions is the key issue in the development. Estimation of the spectra is also important for research in astrophysics and elementary particle physics.

A number of studies have been carried out to build the model. The most of the earlier work was devoted to the construction of semi-empirical or analytical models. For instance, O'Brien *et al.* developed a deterministic code LUN (5) based on an analytical two-component solution of the Boltzmann transport equation, which is employed in the route-dose calculation code CARI-6 (3). However, most this research has shifted to the development of Monte Carlo code that can be used in the simulation of atmospheric propagation of cosmic rays, owing to the dramatic improvement of computer performance in the last decade. Several simulation codes such as CORSIKA (6), COSMOS (7), PLANETOCOSMICS (8) and FLUKA (9, 10) were developed or used for this purpose. Some of their simulation results, e.g. ref. (11), proved their excellent ability to reproduce measured neutron spectra at flight altitudes, which are the most important quantity to be reproduced in route-dose calculation. However, those Monte Carlo codes are rarely incorporated directly into a route-dose calculation

code, since it is extremely time-consuming to perform Monte Carlo simulation of the cosmic-ray propagation for each route-dose calculation even using the latest computer. For example, it takes approximately half a day to calculate terrestrial cosmic-ray spectra at a certain location by Monte Carlo simulation using our parallel computer with 24 CPUs, and route-dose calculation directly based on the Monte Carlo simulation is expected to be much more time-consuming due to the variety of operational flight conditions. Assumption or parameterization is thus required to allow the Monte Carlo-obtained spectra to be used in route-dose calculation.

With these problems in mind, we calculated the terrestrial cosmic-ray spectra by performing the Monte Carlo simulation of cosmic-ray propagation in the atmosphere by the Particle and Heavy Ion Transport code System PHITS (12) coupled with the nuclear data library JENDL-High-Energy File (JENDL/HE) (13, 14). Based on a comprehensive analysis of the simulation results, we proposed an analytical model for estimating the atmospheric cosmic-ray spectra for neutrons, protons, helium ions, muons, electrons, positrons and photons applicable to any global conditions at altitudes below 20 km. The model was designated PARMA, or PHITS-based Analytical Radiation Model in the Atmosphere. The details of the simulation procedure together with the calculated cosmic-ray neutron spectra were published in our previous paper (15). This paper therefore focuses on describing the results for other particles, including the derivation and verification of PARMA for these particles.

## MONTE CARLO SIMULATION

### Simulation Procedure

The simulation procedure for the atmospheric propagation of cosmic rays is basically the same as that described in our previous paper (15) except for the source-term determination. In the simulation, the atmosphere was divided into 28 concentric spherical shells, and its maximum altitude was assumed to be 86 km. The densities and temperatures of each shell were determined by referring to the U.S. Standard Atmosphere 1976. Note that argon was replaced by the atom with the same mass number, calcium, in our simulation, since JENDL/HE did not include the data for argon. The Earth was represented as a sphere with a radius of 6378.14 km, and its composition was presumed to be the same as that of the air at sea level to obtain the atmospheric cosmic-ray spectra under the ideal condition, i.e. without the disturbance of the local geometry effect. The particles reaching 1000 g/cm<sup>2</sup> below the ground level were discarded in the simulation to reduce the computational time. Note that the composition of the soil significantly influences the neutron spectra at the ground level (16, 17), and we analyzed the dependence of the spectra on the composition by changing the water density in the ground (15). However, the effects of the composition on the other particle spectra are expected to be much smaller compared to the neutron case, since there are few albedo particles other than neutrons.

In the simulation, cosmic rays were incident from the top of the atmosphere assumed in the virtual Earth system, i.e. from the altitude of 86 km. The galactic cosmic-ray (GCR) protons and heavy ions with energies and charges up to 200 GeV/nucleon and 28 (nickel), respectively, were considered as the source particles. The GCR spectra around the Earth can be estimated from their local interstellar (LIS) spectra, considering the modulation due to the solar wind magnetic field, so-called solar

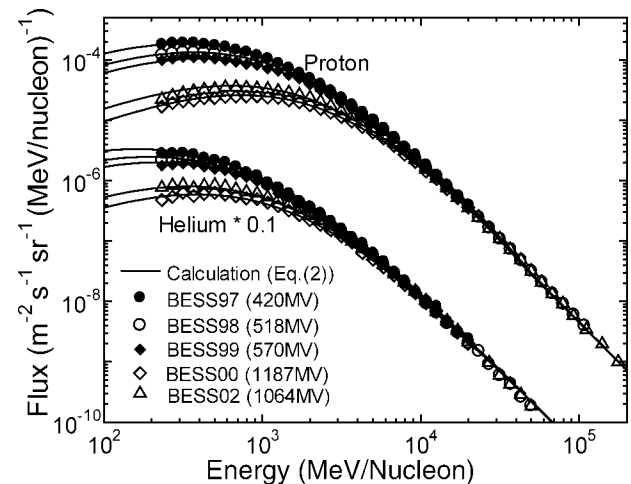


**FIG. 1.** Calculated GCR proton and helium-ion spectra above the Earth's atmosphere in comparison with the experimental data obtained by the BESS spectrometer during the last solar period. The values in the parentheses indicate the force field potential calculated from several neutron monitor count rates at each experimental date.

modulation. In the determination of the source particle spectra in our simulation, we employed the LIS spectra calculated by the Nymmik model (18) coupled with modified parameters. The solar modulation was considered based on the force field formalism (19, 20), using the force field potential that is occasionally called the heliocentric potential (5, 21).

Figure 1 shows the calculated GCR proton and helium-ion spectra above the Earth's atmosphere compared to the corresponding experimental data obtained by the BESS spectrometer (22) during the last solar period. The numerical values of the force field potential at each experimental date were calculated from the count rates of several neutron monitors located all over the world (23); their relationship will be presented in a future paper. Note that our calculation procedure for estimating the numerical value of the force field potential is different from that for the heliocentric potential (5), although the results are close to each other. We therefore adopted the name "force field potential" instead of "heliocentric potential" in this paper to prevent confusion between the two quantities. It is found from the graph that the lower energy fluxes decrease with an increase in the modulation potential, and the calculation can reproduce the experimental tendency very well. We therefore concluded that the calculated GCR spectra are precise enough to be used in making the source determination in the atmospheric propagation simulation of cosmic rays.

The Monte Carlo simulations were carried out for five force field potentials—400, 600, 900, 1200 and 1800 MV—and 18 geomagnetic fields with the vertical cut-off rigidities from 0 to 17 GV. The azimuth and zenith dependences of the cut-off rigidity were considered by assuming that the geomagnetism can be simply expressed by a dipole magnet, as described in ref. (17).

The atmospheric propagation of the incident cosmic rays and their associated cascades was simulated by the PHITS code, which can deal with the transport of all kinds of hadrons and heavy ions with energies up to 200 GeV/nucleon. PHITS can also treat the production, transport and decay of photons, electrons, positrons, pions, muons, kaons and various resonant states. In the simulation, two models, JENDL/HE and INC, the widely used model of the intranuclear cascade (24), were alternatively employed for simulating nuclear reactions induced by neutrons and protons below 3 GeV. An advantage of JENDL/HE compared to INC is that it can precisely calculate the yields of high-energy secondary particles knocked out from light ions such as nitrogen and oxygen, which are the dominant components of the atmosphere. Owing to this property, the simulation using JENDL/HE can reproduce the experimental data of cosmic-ray neutron spectra very well even near sea level, as shown in our

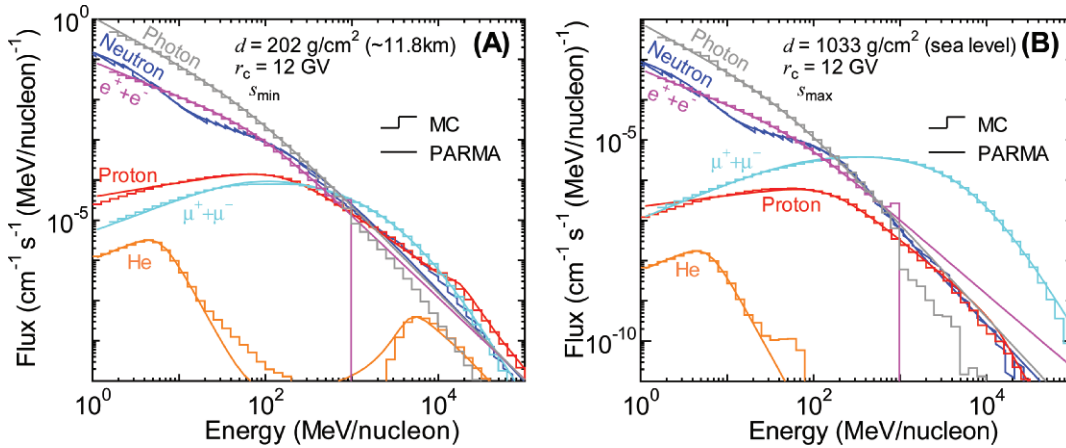


**FIG. 2.** Calculated cosmic-ray spectra at a typical flight altitude (A) and near sea level (B). The values of  $d$  and  $r_c$  are the atmospheric depth and the cut-off rigidity, respectively, while  $s_{\min}$  and  $s_{\max}$  indicate the solar minimum and maximum conditions with the force field potential 400 and 1200 MV, respectively. These notations are also used in the other figures.

previous paper (15). However, the current version of JENDL/HE written in PHITS-readable format did not include the pion-production channels, and consequently the spectra of pions and the particles associated with their decay—muons, electrons, positrons and photons—could not be determined precisely by the simulation. We therefore decided to adopt the results obtained by the simulation employing JENDL/HE for neutron, proton and helium-ion spectra and the simulation employing INC for muon, electron, positron and photon spectra in the analysis throughout this paper.

### Results of the Simulation

As examples of the simulation results, the cosmic-ray spectra at a typical flight altitude and near sea level are shown in Fig. 2. The statistical uncertainties in the values obtained by the simulation are generally small, less than approximately 5% and 20% for the flight altitude and sea-level data, respectively, except for helium-ion spectra. The corresponding spectra calculated by the analytical model proposed in the next section, PARMA, are also plotted in the figure. The discussions about the comparison between the results obtained by the Monte Carlo simulation and PARMA are given in the next section.

In general, the fluxes of the terrestrial cosmic rays at flight altitude are approximately 100 times larger than those near sea level except for those of muons. This tendency is consistent with the well-known fact that dose rates at conventional flight altitudes are approximately 100 times higher than those at sea level. The muon flux does not increase with rising altitude very much in comparison to other particles because of their strong penetrability in the atmosphere.

The energy ranges of the electron and positron spectra obtained by the simulation have an upper limit of 1 GeV, since the current version of PHITS cannot handle the transport of electrons and positrons above that energy. When such particles are created in the PHITS calculation, their consequent transports are simulated under the assumption that the energy of the produced particle is equal to 1 GeV, and its importance is weighted by the ratio of the real energy to 1 GeV.

### Comparison with Experimental Data

To examine the usefulness of the calculated cosmic-ray spectra in dose estimation, it is ideal to compare the angular-integrated spectra obtained by Monte Carlo simulation with the corresponding experimental data, as shown in our previous paper dealing with neutrons. In the cases of other particles, however, there are few experimental data that can be used for this purpose, since most of these measurements have been performed for

elucidating angular-differential spectra, this information being of prime importance in astrophysics and elementary particle physics. We therefore compared simulated and experimental angular-differential spectra to verify the accuracy of the Monte Carlo simulation.

The results of the comparisons are shown in Fig. 3. Panel A shows the angular-integrated neutron spectra in the unit of  $\text{cm}^{-2} \text{s}^{-1} \text{lethargy}^{-1}$ , which had been reported in our previous paper (15) in a different unit, in comparison with the measurement (25). Panels B to F, respectively, show the Monte Carlo-obtained proton, muon, photon and electron spectra for the vertical direction in the unit of  $\text{cm}^{-2} \text{s}^{-1} \text{sr}^{-1} \text{MeV}^{-1}$ , plotted together with the corresponding measured data (26–34) under a variety of experimental conditions. Excellent agreement between the calculated and measured spectra was observed except for the electron data, indicating the adequacy of the assumptions adopted in the Monte Carlo simulation. We therefore concluded that the cosmic-ray spectra estimated by our simulation are precise enough to be subjected to systematic analysis for developing an analytical model of these spectra. The discrepancy in the electron spectra is presumed to be attributable to the assumption made in the treatment of high-energy electron transport adopted in PHITS, as described before. The slight disagreement observed in the photon spectra at sea level is probably due to the effect of photons emitted from radioisotopes, which was not considered in our simulation.

## ANALYTICAL MODEL: PARMA

### General Description of PARMA

The analytical model proposed in this section enables us to estimate the cosmic-ray proton, helium-ion, electron, positron, photon and muon spectra with energies from 1 MeV to 200 GeV. The unit of the obtained spectra is  $\text{cm}^{-2} \text{s}^{-1} \text{MeV}^{-1}$ , supplying the force field potential in MV, the vertical cut-off rigidity in GV, and the kinetic energy in MeV except for the case of helium ions, where the kinetic energy is given in MeV/nucleon to estimate its spectra in  $\text{cm}^{-2} \text{s}^{-1} (\text{MeV/nucleon})^{-1}$ . Although the full two-dimensional distribution of the cut-off rigidity was considered in the PHITS simulation, we simply adopted the vertical cut-off rigidity as an index for accessing the simulation results. The associating errors are expected to be small except for the magnetic equator region, as discussed in ref. (5). This

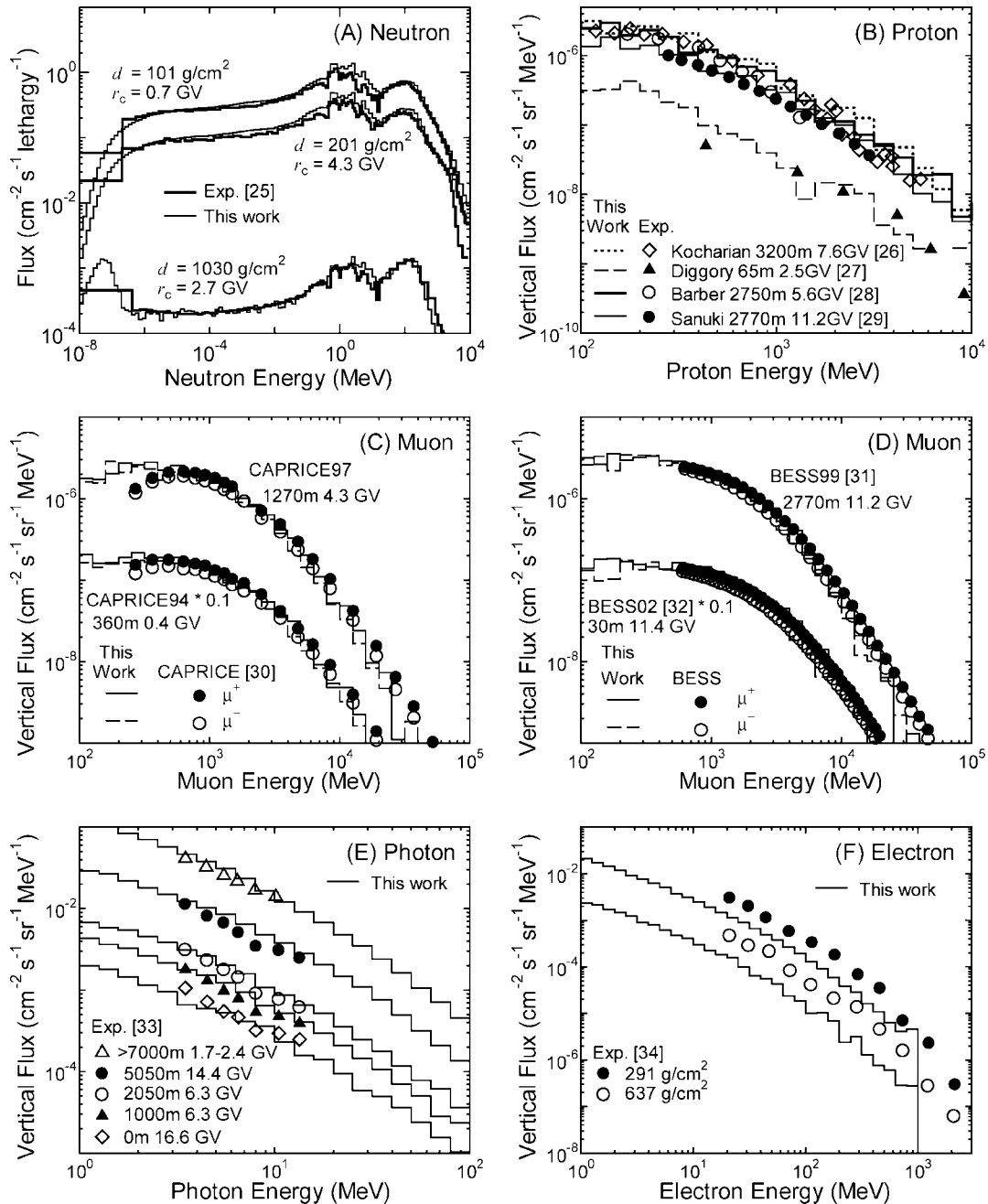


**FIG. 3.** Comparison between the calculated and experimental cosmic-ray spectra in the atmosphere. Panel A shows the angular-integrated spectra in the unit of  $\text{cm}^{-2} \text{s}^{-1} \text{lethargy}^{-1}$ , while panels B–F show the spectra for the vertical direction in the unit of  $\text{cm}^{-2} \text{s}^{-1} \text{sr}^{-1} \text{MeV}^{-1}$ .

model coupled with that for neutrons proposed in our previous paper (15) was given the name PARMA.

In the development of PARMA, the Monte Carlo-obtained spectra for the force field potentials 400 and 1200 MV were regarded as the data for the solar minimum and maximum conditions, respectively, although the highest force field potential adopted in our Monte Carlo simulation was 1800 MV. The data for the other force field potentials were used only for the determination of the solar-modulation dependence of the secondary particle fluxes, as dis-

cussed later in this section. The Monte Carlo-obtained spectra at the altitudes above 20 km ( $\sim 59 \text{ g/cm}^2$ ) were not considered in the derivation of PARMA for the following two reasons: (1) the equilibrium between the numbers of incoming and outgoing particles, which is a necessary condition for calculating lower-energy particle fluxes by our model, is not established at the higher altitudes, and (2) commercial flights never exceed an altitude of 20 km. Thus the applicable altitude range of PARMA is limited to 20 km.

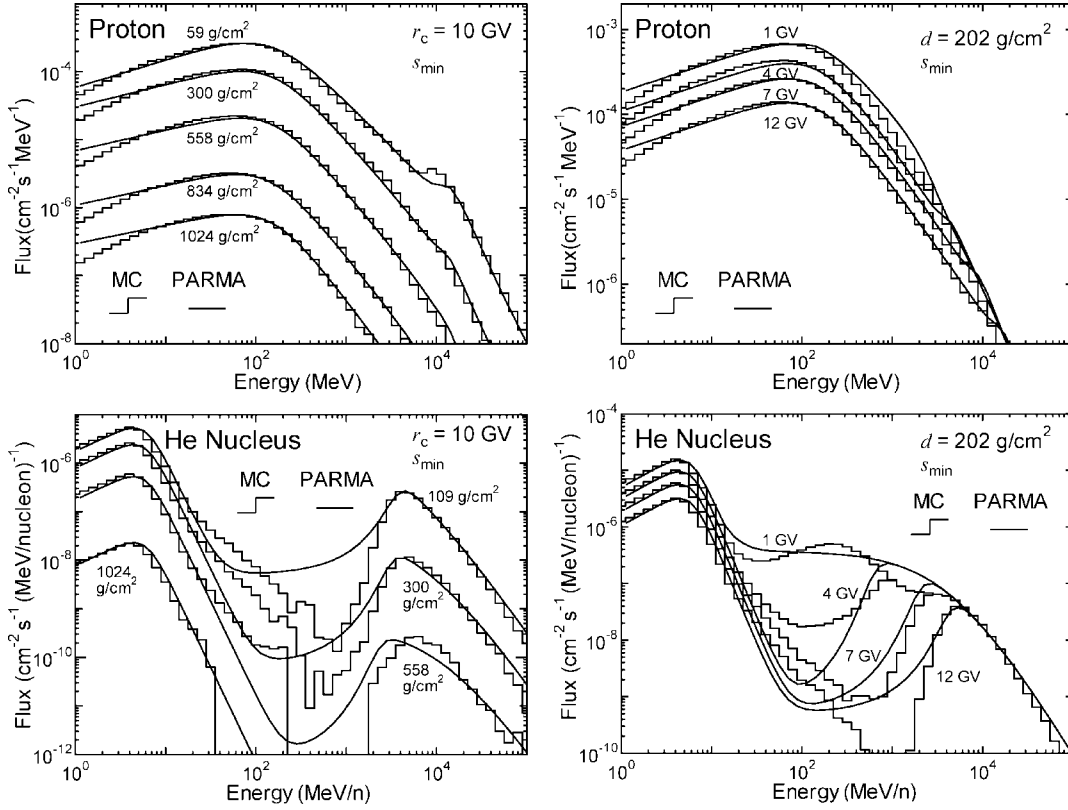


**FIG. 4.** Comparison between the cosmic-ray proton and helium-ion spectra obtained by our Monte Carlo simulation and PARMA. The left and right panels show the atmospheric depth and the cut-off rigidity dependence of the spectra, respectively.

### Consideration of Proton and Helium-Ion Spectra

Figure 4 shows the cosmic-ray proton and helium-ion spectra obtained by the Monte Carlo simulation, together with the corresponding data calculated by PARMA. The left and right panels show the atmospheric depth and the

**TABLE 1**  
Numerical Values of the Parameters  $a$  used in Eqs. (1) to (3) and (11) to (13) for Estimating the Atmospheric Proton and Helium-Ion Spectra

Parameter	Protons	Helium ions
$a_1$ ( $\text{cm}^2 \text{g}^{-1} \text{MeV/nucleon}$ )	2.12	17.6
$a_2$	0.445	0.438
$a_3$ ( $\text{cm}^2 \text{g}^{-1}$ )	0.0101	0.0121
$a_4$ ( $\text{cm}^2 \text{g}^{-1}$ )	0.0396	0.0434
$a_5$	2.924	1.841
$a_6$	2.708	2.646
$a_7$ ( $\text{s}^{-1} \text{m}^{-2} \text{sr}^{-1} \text{GV}^{-1}$ )	$1.27 \times 10^4$	$2.36 \times 10^3$
$a_8$ ( $\text{s}^{-1} \text{m}^{-2} \text{sr}^{-1} \text{GV}^{-1}$ )	$4.83 \times 10^3$	432
$a_9$ ( $\text{MeV/nucleon}$ )	$3.28 \times 10^4$	$6.06 \times 10^3$
$a_{10}$ ( $\text{MeV/nucleon}$ )	$7.44 \times 10^3$	$2.41 \times 10^3$
$a_{11}$	3.46	3.33
$a_{12}$	1.68	11.7
$a_{13}$	1.37	0.967
$a_{14}$ ( $\text{cm}^2 \text{g}^{-1} \text{MeV/nucleon}$ )	2.07	3.20
$a_{15}$ ( $\text{MeV/nucleon}$ )	108	15.0
$a_{16}$ ( $\text{MeV/nucleon}$ )	$2.30 \times 10^3$	853

vertical cut-off rigidity dependences of the spectra, respectively. It is found from the data in the figure that the spectra can be divided into higher- and lower-energy components, although they are not clearly distinguished in the case of protons. The two components consist predominantly of the primary cosmic rays and their secondary particles produced in the atmosphere, respectively. The switching energy between the two components depends on the cut-off rigidity, as discussed later in this section. We first established the mathematical functions to estimate the primary and secondary particle spectra separately and then constructed analytical models for predicting the whole spectrum by combining them.

### Primary Particle Spectra for Protons and Helium Ions

Considering the energy loss and nuclear interactions in the atmosphere, the primary proton and helium-ion spectra  $\Phi_{\text{pri}}$  can be assumed to be expressed by

$$\begin{aligned} \Phi_{\text{pri}}(s, d, E) &= \Phi_{\text{TOA}}(s, E + a_1 d) \\ &\times [a_2 \exp(-a_3 d) + (1 - a_2) \exp(-a_4 d)]. \end{aligned} \quad (1)$$

where  $s$ ,  $d$  and  $E$  denote the force field potential, the atmospheric depth and the kinetic energy per nucleon, re-

spectively, and  $\phi_{\text{TOA}}$  is the spectra at the top of the atmosphere. The effect of the magnetosphere was not considered in this equation and will be taken into account in the equation for combining the primary spectra with the secondary one, i.e. in Eq. (11) proposed later in this section.

The parameter  $a_1$  is related to the particle stopping power of the atmosphere, and consequently  $E + a_1 d$  indicates the kinetic energy at the top of the atmosphere. The two exponential decay terms represent the decrease in the primary-particle fluxes due to nuclear interactions, and the parameters  $a_2$  to  $a_4$  are related to primary particle macroscopic cross sections in the atmosphere. Hence the parameters  $a_i$  should depend on the particle energy in a complicated manner, but we assumed that they were constant for each particle and determined their numerical values from the least-squares fitting of their high-energy spectra (above several GeV, depending of the cut-off rigidity) as obtained by the Monte Carlo simulation, assuming that there is no secondary particle in such a high-energy region. The results of the fitting are summarized in Table 1.

In the least-squares fitting,  $\phi_{\text{TOA}}$  was obtained from the LIS spectra calculated by the Nymmik model (18) coupled with modified parameters, considering the solar modulation based on the force field formalism, as described in the previous section. It can be written as

$$\phi_{\text{TOA}}(s, E) = \frac{C(E_{\text{LIS}})[\beta(E_{\text{LIS}})]^{a_5} \left[ \frac{R(E)}{R(E_{\text{LIS}})} \right]^2}{[R(E_{\text{LIS}})]^{a_6}}, \quad (2)$$

where  $E_{\text{LIS}}$  is the kinetic energy at LIS,  $\beta$  is the speed of the particle relative to light, and  $R$  is the rigidity of the particle in GV, which can be obtained from the equation  $R = 0.001 \times \sqrt{(AE)^2 + 2AE_m E/Z}$ , where  $A$ ,  $Z$  and  $E_m$  are the mass and charge number and the rest mass of the particle, respectively. The former part of the right side of Eq. (2),  $C\beta^{a_5}R^{-a_6}$ , expresses the LIS spectra, while the latter does the effect of the solar modulation based on the force field formalism. Note that  $E$  and  $E_m$  should be supplied in MeV/nucleon and MeV, respectively. Based on the force field formalism,  $E_{\text{LIS}}$  can be simply determined by  $E + sZ/A$ , where  $s$  is the force field potential expressed in MV.

In the original Nymmik model, the parameter  $C$  is regarded as constant. However, Eq. (2) coupled with a constant  $C$  parameter cannot reproduce the proton and helium-ion spectra at the top of the atmosphere measured with the BESS spectrometer during the variety of the solar-modulation conditions over wide energy ranges very much. We therefore presumed that the parameter  $C$  depends on the particle energy and their relationship can be expressed by the sigmoid function:

$$C(E) = a_7 + \frac{a_8}{1 + \exp[(E - a_9)/a_{10}]}. \quad (3)$$

where  $a_7$  to  $a_{10}$  are constant parameters. The numerical values of  $a_5$ ,  $a_8$ ,  $a_9$  and  $a_{10}$  were determined from the least-squares fitting of the BESS data. In the least-squares fitting,

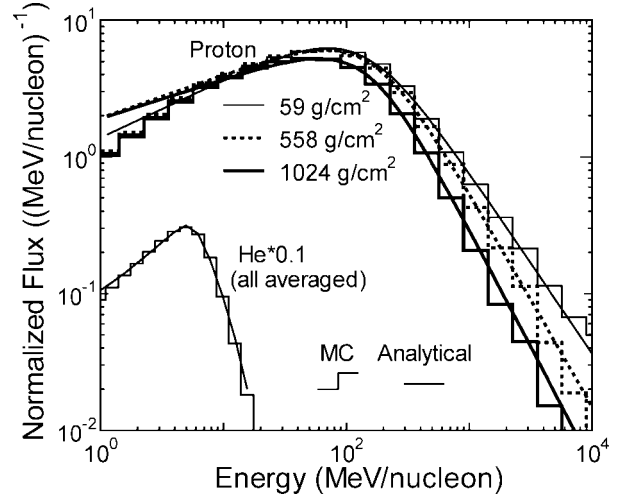


FIG. 5. Normalized proton and helium-ion spectra by their fluxes at the energy of 1 MeV/nucleon.

the parameters  $a_6$  and  $a_7$  were fixed to force  $\phi_{\text{TOA}}$  calculated by Eq. (2) asymptotic to that obtained from the Honda model (35) in the high-energy region. It should be noted that this calculation method was introduced only for reproducing the BESS data and is not fully based on a theoretical model. The results of the fitting are also summarized in Table 1. Note that Eqs. (2) and (3) coupled with the parameters listed in Table 1 give the particle spectra in the unit of  $\text{s}^{-1} \text{m}^{-2} \text{sr}^{-1} \text{GV}^{-1}$ . Thus they should be multiplied by  $(4\pi - \Omega_E) \times (A/Z)/\beta \times 10^{-7}$ , where  $\Omega_E$  is the solid angle of the Earth from a point at the top of the atmosphere in our simulation, to convert that unit into the one used in the least-squares fitting of the terrestrial proton and helium-ion spectra— $\text{cm}^{-2} \text{s}^{-1} (\text{MeV/nucleon})^{-1}$ . The numerical value of  $\Omega_E$  is equal to  $1.675\pi$ .

### Secondary Particle Spectra for Protons and Helium Ions

To estimate the influence of the global conditions on the relative shapes of the secondary spectra, we normalized the spectra to their fluxes at the energy of 1 MeV/nucleon, at which the contributions of the primary particles to the fluxes are almost negligible. By analyzing the normalized spectral shape, we found that the proton data depend only on the atmospheric depth and are almost independent of the cut-off rigidity and the force field potential and that the data for helium ions are independent of all global conditions. Figure 5 shows examples of the normalized spectra. The proton data shown in the figure were obtained by averaging over all Monte Carlo results at all the altitudes, while the data for helium ions were the mean spectra of all global conditions. It is found from the data in the figure that the normalized spectra in lower- and higher-energy regions can be expressed simply by power functions of the particle energy.

Based on these considerations, we introduced the following function to estimate the secondary particle spectra  $\phi_{\text{sec}}$ :

**TABLE 2**  
**Numerical Values of the Coefficients of Third Order of the Polynomial Function—the Parameters  $c$  in Eq. (5)—Obtained from the Least-Squares Fittings**

Parameter		$c_{i1}$	$c_{i2}$	$c_{i3}$	$c_{i4}$
Protons	$b_1$	1.26	0.00323	$4.81 \times 10^{-6}$	$2.28 \times 10^{-9}$
	$b_2$	0.438	$-5.58 \times 10^{-4}$	$7.84 \times 10^{-7}$	$-3.87 \times 10^{-10}$
	$b_3$	$1.81 \times 10^{-4}$	$-5.18 \times 10^{-7}$	$7.59 \times 10^{-10}$	$-3.82 \times 10^{-13}$
	$b_4$	1.71	$7.16 \times 10^{-4}$	$-9.32 \times 10^{-7}$	$5.27 \times 10^{-10}$
Helium ions	$b_1$	1.00			
	$b_2$	0.881			
	$b_3$	$1.80 \times 10^{-4}$			
	$b_4$	4.77			
Electrons	$b_1$	6.44	0.0266	$-5.97 \times 10^{-5}$	$4.39 \times 10^{-8}$
	$b_2$	-0.894	$-3.58 \times 10^{-4}$	$2.37 \times 10^{-7}$	$5.39 \times 10^{-11}$
	$b_3$	0.00231	$8.07 \times 10^{-6}$	$-2.00 \times 10^{-8}$	$1.89 \times 10^{-11}$
	$b_4$	1.13	$6.64 \times 10^{-4}$	$-1.04 \times 10^{-6}$	$3.13 \times 10^{-10}$
Positrons	$b_1$	2.29	0.0124	$-2.94 \times 10^{-5}$	$2.08 \times 10^{-8}$
	$b_2$	-0.455	$-7.14 \times 10^{-4}$	$1.17 \times 10^{-6}$	$-5.13 \times 10^{-10}$
	$b_3$	0.00387	$-5.82 \times 10^{-6}$	$6.76 \times 10^{-9}$	$2.93 \times 10^{-12}$
	$b_4$	1.28	$8.82 \times 10^{-4}$	$-1.31 \times 10^{-6}$	$4.22 \times 10^{-10}$
Photons	$b_1$	15.8	0.00963	$-2.22 \times 10^{-5}$	$2.53 \times 10^{-8}$
	$b_2$	-1.25	$8.44 \times 10^{-4}$	$-2.14 \times 10^{-6}$	$1.36 \times 10^{-9}$
	$b_3$	0.0121	$2.47 \times 10^{-5}$	$-5.33 \times 10^{-8}$	$2.79 \times 10^{-11}$
	$b_4$	0.825	0.00134	$-2.18 \times 10^{-6}$	$1.15 \times 10^{-9}$

*Note.* The parameters  $b$  for helium ions are assumed to be independent of the atmospheric depth, i.e.  $c_{i2} = c_{i3} = c_{i4} = 0$ .

$$\phi_{\text{sec}}(s, r_c, d, E) = \Phi_N(s, r_c, d) \frac{b_1(d)E^{b_2(d)}}{1 + b_3(d)E^{b_4(d)}}, \quad (4)$$

where  $\Phi_N$  is the flux used for the normalization of the spectra, i.e. flux at 1 MeV,  $r_c$  is the cut-off rigidity, and  $b_i$  are free fitting parameters. For  $b_3 \ll 1$ ,  $\phi_{\text{sec}}$  is proportional to the power functions  $E^{b_2}$  and  $E^{b_2-b_4}$  in lower- and higher-energy regions, respectively. The parameters  $b_i$  for reproducing the proton spectra are assumed to be dependent on  $d$ , while those for the helium-ion spectra are assumed to be constant. If  $\phi_{\text{sec}}$  can be fitted perfectly by the equation, then  $b_1$  should be equal to 1. However,  $b_1$  was also regarded as a fitting parameter in the case of protons, since the normalized proton spectra in the very low-energy region could not be expressed by a simple power function. The numerical values of  $b_i$  were determined from the least-squares fitting of the normalized spectra. The curves resulting from the fitting curves are also plotted in Fig. 5, and they clearly demonstrate the ability of the equation to reproduce the simulation results.

For expressing the dependences of  $b_i$  for protons on the atmospheric depth  $d$ , we simply introduced the third-order polynomial function:

$$b_i(d) = c_{i1} + c_{i2}d + c_{i3}d^2 + c_{i4}d^3, \quad (5)$$

where the parameters  $c_{ij}$  are the fitting constants. Table 2 summarizes the numerical values of the parameters  $c_{ij}$  obtained from the least-squares fitting of the  $b_i$  data together with those of the constant  $b_i$  parameters for reproducing the secondary helium-ion spectra.

The flux used for the normalization  $\Phi_N$  can be obtained

in the same manner as the low-energy atmospheric neutron fluxes, whose calculation procedure was described in detail in our previous paper (15). Since equilibrium between the numbers of incoming and outgoing particles is almost established at low energies,  $\Phi_N$  for the solar minimum condition,  $\Phi_{N\text{min}}$ , can be expressed by

$$\begin{aligned} \Phi_{N\text{min}}(r_c, d) &= g_{1\text{min}}(r_c) \{ \exp[-g_{2\text{min}}(r_c)d] \\ &\quad - g_{3\text{min}}(r_c) \exp[-g_{4\text{min}}(r_c)d] \}, \quad (6) \end{aligned}$$

where  $g_1$  to  $g_4$  are parameters depending on the cut-off rigidity  $r_c$ . The normalization flux for the solar maximum condition,  $\Phi_{N\text{max}}$ , can be also estimated from Eq. (6) by replacing the subscript “min” with “max” in the equation. For expressing the dependence of  $g_i$  on  $r_c$ , we introduced the sigmoid function coupled with the linear term:

$$g_i(r_c) = h_{i1} + h_{i2}r_c + \frac{h_{i3}}{1 + \exp[(r_c - h_{i4})/h_{i5}]}, \quad (7)$$

where  $h_{i1}$  to  $h_{i5}$  are free parameters. The numerical values of the parameters  $h_{ij}$  for the solar minimum and maximum conditions were determined from the least-squares fitting of the Monte Carlo-obtained  $\Phi_N$  data for the force field potentials 400 and 1200 MV, respectively. The results of this least-squares fitting are summarized in Table 3. It should be noted that the cosmic-ray spectra below the altitude of 20 km are almost independent of the cut-off rigidity for  $r_c < 1$  GV, since incident cosmic rays with rigidity below 1 GV together with their secondary particles generally cannot

**TABLE 3**  
**Numerical Values of the Parameters  $h$  used in Eq. (7) for Expressing the Cut-off Rigidity Dependence of the  $g$  Data**

Parameter		$h_{i1}$	$h_{i2}$ (GV <sup>-1</sup> )	$h_{i3}$	$h_{i4}$ (GV)	$h_{i5}$ (GV)
Protons	$g_{1min}$ (cm <sup>-2</sup> s <sup>-1</sup> )	0.00244	$-6.03 \times 10^{-5}$	0.00220	6.68	0.932
	$g_{1max}$ (cm <sup>-2</sup> s <sup>-1</sup> )	0.00255	$-7.18 \times 10^{-5}$	0.00146	6.92	0.994
	$g_{2min}$ (cm <sup>2</sup> g <sup>-1</sup> )	0.00779	$-9.58 \times 10^{-6}$	$6.22 \times 10^{-4}$	7.78	1.85
	$g_{2max}$ (cm <sup>2</sup> g <sup>-1</sup> )	0.00768	$-2.41 \times 10^{-6}$	$6.64 \times 10^{-4}$	7.75	1.94
	$g_{3min}$	0.963	0.00160	-0.0712	2.23	0.788
	$g_{3max}$	0.974	0.00106	-0.0214	3.01	0.918
	$g_{4min}$ (cm <sup>2</sup> g <sup>-1</sup> )	0.00781	$9.71 \times 10^{-11}$	$8.24 \times 10^{-4}$	8.51	2.31
	$g_{4max}$ (cm <sup>2</sup> g <sup>-1</sup> )	0.00735	$2.56 \times 10^{-5}$	0.00125	8.19	2.94
	$g_5$	0.191	0.0703	-0.645	2.03	1.30
	$g_6$ (cm <sup>2</sup> g <sup>-1</sup> )	$5.71 \times 10^{-4}$	$6.13 \times 10^{-6}$	$5.47 \times 10^{-4}$	1.11	0.837
Helium ions	$g_{1min}$ (cm <sup>-2</sup> s <sup>-1</sup> )	$-2.00 \times 10^{-5}$	$1.79 \times 10^{-6}$	$9.01 \times 10^{-5}$	6.87	4.82
	$g_{1max}$ (cm <sup>-2</sup> s <sup>-1</sup> )	$-5.21 \times 10^{-5}$	$3.81 \times 10^{-6}$	$9.88 \times 10^{-5}$	8.26	3.81
	$g_{2min}$ (cm <sup>2</sup> g <sup>-1</sup> )	0.00566	$7.51 \times 10^{-5}$	0.00275	8.20	4.96
	$g_{2max}$ (cm <sup>2</sup> g <sup>-1</sup> )	0.00524	$9.97 \times 10^{-5}$	0.00309	8.21	4.67
	$g_{3min}$	0.925	0.00260	-0.828	-0.637	1.90
	$g_{3max}$	0.918	0.00332	-0.133	2.26	1.41
	$g_{4min}$ (cm <sup>2</sup> g <sup>-1</sup> )	0.00893	$-5.75 \times 10^{-5}$	$7.47 \times 10^{-4}$	5.53	1.34
	$g_{4max}$ (cm <sup>2</sup> g <sup>-1</sup> )	0.00831	$-3.19 \times 10^{-5}$	$9.70 \times 10^{-4}$	7.85	3.74
	$g_5$	0.212	0.0769	-0.620	2.47	1.43
	$g_6$ (cm <sup>2</sup> g <sup>-1</sup> )	$5.57 \times 10^{-4}$	$-1.81 \times 10^{-5}$	$4.56 \times 10^{-4}$	0.943	1.25
Electrons	$g_{1min}$ (cm <sup>-2</sup> s <sup>-1</sup> )	0.0466	-0.00111	0.0234	6.80	2.69
	$g_{1max}$ (cm <sup>-2</sup> s <sup>-1</sup> )	0.0125	$4.30 \times 10^{-4}$	0.0410	9.16	4.35
	$g_{2min}$ (cm <sup>2</sup> g <sup>-1</sup> )	0.00690	$-8.92 \times 10^{-6}$	$6.86 \times 10^{-4}$	7.31	3.51
	$g_{2max}$ (cm <sup>2</sup> g <sup>-1</sup> )	0.00648	$9.61 \times 10^{-6}$	$8.85 \times 10^{-4}$	8.93	4.22
	$g_{3min}$	1.04	0.00554	-0.0808	4.49	1.56
	$g_{3max}$	1.06	0.00416	-0.0513	5.70	2.11
	$g_{4min}$ (cm <sup>2</sup> g <sup>-1</sup> )	0.0161	$-1.64 \times 10^{-10}$	0.00253	4.61	3.42
	$g_{4max}$ (cm <sup>2</sup> g <sup>-1</sup> )	0.0166	$-3.07 \times 10^{-5}$	0.00104	6.63	1.89
	$g_5$	0.464	0.0255	-0.330	3.79	1.33
	$g_6$ (cm <sup>2</sup> g <sup>-1</sup> )	$-8.21 \times 10^{-5}$	$-1.07 \times 10^{-5}$	0.00103	1.19	4.86
Positrons	$g_{1min}$ (cm <sup>-2</sup> s <sup>-1</sup> )	0.0284	$-7.92 \times 10^{-4}$	0.00963	6.43	2.16
	$g_{1max}$ (cm <sup>-2</sup> s <sup>-1</sup> )	0.00702	$2.24 \times 10^{-4}$	0.0223	8.92	4.29
	$g_{2min}$ (cm <sup>2</sup> g <sup>-1</sup> )	0.00655	$6.30 \times 10^{-6}$	0.00119	6.88	4.54
	$g_{2max}$ (cm <sup>2</sup> g <sup>-1</sup> )	0.00633	$1.63 \times 10^{-5}$	0.00109	8.61	4.47
	$g_{3min}$	1.07	0.00536	-0.240	1.92	2.87
	$g_{3max}$	1.07	0.00532	-0.0678	5.37	1.47
	$g_{4min}$ (cm <sup>2</sup> g <sup>-1</sup> )	0.0170	$-6.99 \times 10^{-6}$	0.00255	4.84	3.08
	$g_{4max}$ (cm <sup>2</sup> g <sup>-1</sup> )	0.0167	$-2.52 \times 10^{-8}$	0.00213	6.48	3.62
	$g_5$	0.463	0.0255	-0.329	3.78	1.33
	$g_6$ (cm <sup>2</sup> g <sup>-1</sup> )	$-7.12 \times 10^{-5}$	$-1.13 \times 10^{-5}$	0.00102	1.04	4.85
Photons	$g_{1min}$ (cm <sup>-2</sup> s <sup>-1</sup> )	0.528	-0.0146	0.208	5.86	2.58
	$g_{1max}$ (cm <sup>-2</sup> s <sup>-1</sup> )	0.150	0.00277	0.414	8.70	4.69
	$g_{2min}$ (cm <sup>2</sup> g <sup>-1</sup> )	0.00532	$4.99 \times 10^{-5}$	0.00271	7.90	7.21
	$g_{2max}$ (cm <sup>2</sup> g <sup>-1</sup> )	0.00523	$5.20 \times 10^{-5}$	0.00249	9.01	7.25
	$g_{3min}$	1.07	0.00291	-0.145	0.00622	3.42
	$g_{3max}$	1.06	0.00300	-0.0318	4.84	1.75
	$g_{4min}$ (cm <sup>2</sup> g <sup>-1</sup> )	0.0139	$-1.71 \times 10^{-5}$	0.00135	5.38	2.16
	$g_{4max}$ (cm <sup>2</sup> g <sup>-1</sup> )	0.0140	$-2.47 \times 10^{-5}$	$7.20 \times 10^{-4}$	7.27	1.70
	$g_5$	0.464	0.0255	-0.329	3.79	1.33
	$g_6$ (cm <sup>2</sup> g <sup>-1</sup> )	$-5.75 \times 10^{-5}$	$-1.19 \times 10^{-5}$	$9.58 \times 10^{-4}$	1.41	4.67

reach these lower altitudes. Hence we regarded  $g_i$  for  $r_c < 1$  GV as the constant that obtained from Eq. (7) by substituting 1.0 for  $r_c$ ; i.e., the minimum of the applicable cut-off rigidity in Eq. (7) is 1 GV. This limitation is also applied in Eq. (17) defined later in this paper.

To determine  $\Phi_N$  for arbitrary solar conditions, we assumed that the dependence of  $\Phi_N$  on the force field potential  $s$  can be written as

$$\Phi_N(s, r_c, d) = f_1(r_c, d) + f_2(r_c, d)g_5^{f_3(r_c, d)}, \quad (8)$$

where  $f_i$  are the parameters depending on  $r_c$  and  $d$ . The power index of  $s$ ,  $f_3(r_c, d)$ , generally increases with the rise of the atmospheric depth. We assumed that their relation can be represented by the linear function

$$f_3(r_c, d) = g_5(r_c) + g_6(r_c)d, \quad (9)$$

where  $g_5$  and  $g_6$  are parameters depending on  $r_c$  as ex-



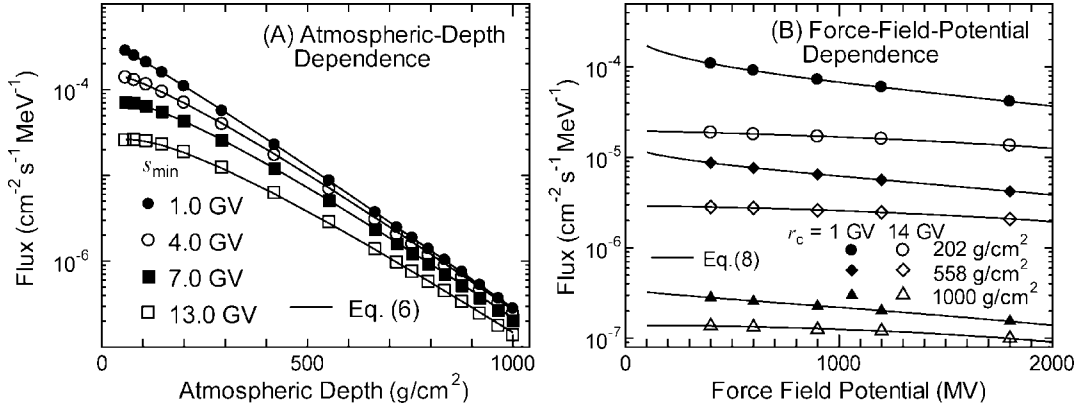


FIG. 6. Proton fluxes at 1 MeV/nucleon,  $\Phi_N$ , as a function of (panel A) atmospheric depth and (panel B) force field potential.

pressed by Eq. (7). The numerical values of the parameters  $h_{s_j}$  and  $h_{e_j}$  were obtained from the least-squares fitting of the Monte Carlo data of  $\Phi_N$  for all force field potentials—400, 600, 900, 1200 and 1800 MV. The results of this least-squares fitting are also provided in Table 3. The parameters  $f_1(r_c, d)$  and  $f_2(r_c, d)$  were determined by solving the simultaneous equations

$$\begin{aligned} \Phi_{N_{\min}}(r_c, d) &= f_1(r_c, d) + f_2(r_c, d)s_{\min}^{f_3(r_c, d)} \quad \text{and} \\ \Phi_{N_{\max}}(r_c, d) &= f_1(r_c, d) + f_2(r_c, d)s_{\max}^{f_3(r_c, d)}, \end{aligned} \quad (10)$$

using  $f_3$ , and  $\Phi_{N_{\min}}$  and  $\Phi_{N_{\max}}$  calculated by Eqs. (9) and (6), respectively. Substituting the obtained  $f_i$  parameters into Eq. (8),  $\Phi_N$  for arbitrary solar conditions can be estimated.

As examples of the calculation results, the dependences of  $\Phi_N$  for proton on the atmospheric depth and the force field potential are shown in Fig. 6 in comparison with the corresponding Monte Carlo-obtained data. It is evident from the figure that the analytical and Monte Carlo results agree closely with each other, indicating the validity of the equations for expressing the changes in  $\Phi_N$ . Substituting  $b_i$  and  $\Phi_N$  calculated by Eqs. (5) and (8), respectively, into Eq. (4), we can analytically estimate the secondary proton and helium-ion spectra.

#### Combining Primary and Secondary Spectra of Protons and Helium Ions

Considering the influence of the cut-off rigidity, the terrestrial cosmic-ray proton and helium-ion spectra  $\phi$  can be estimated from their primary and secondary spectra by

$$\begin{aligned} \phi(s, r_c, d, E) &= \phi_{\text{pri}}(s, d, E)[\tanh\{a_{11}[E/E_{s1}(r_c, d) - 1]\} + 1]/2 \\ &+ \phi_{\text{sec}}(s, r_c, d, E)[\tanh\{a_{12}[1 - E/E_{s2}(r_c, d)]\} + 1]/2, \end{aligned} \quad (11)$$

where  $E_{s_i}$  is the switching energy between the primary and secondary spectra, and  $a_{11}$  and  $a_{12}$  are constant parameters

influencing the smoothness of the spectrum switching. The functions of the hyperbolic tangent were introduced only for expressing the gradual switching of the two spectra, and the form of the equation has little physical meaning. In general, the switching energy for the primary spectra  $E_{s1}$  is equal to that for the secondary spectra  $E_{s2}$  and can be determined from  $r_c$  and  $d$  by the equation

$$E_s(r_c, d) = a_{13}[E_c(r_c) - a_{14}d], \quad (12)$$

where  $a_{13}$  and  $a_{14}$  are constant parameters, and  $E_c$  corresponds to the cut-off energy of the particle at the top of the atmosphere. This can be obtained by  $E_c = [\sqrt{(1000 \times r_c Z)^2 + E_m^2} - E_m]/A$ , where  $r_c$  is given in GV to obtain  $E_c$  in MeV/nucleon. However, it is obvious that most of the lower-energy particles are produced in the atmosphere, i.e. are secondary particles, even for very lower cut-off rigidity cases, and hence we introduced minimum values of  $E_s$  for the primary and secondary particles in the equations

$$\begin{aligned} E_{s1}(r_c, d) &= \max[a_{15}, E_s(r_c, d)] \\ E_{s2}(r_c, d) &= \max[a_{16}, E_s(r_c, d)], \end{aligned} \quad (13)$$

respectively, where  $a_{15}$  and  $a_{16}$  represent the minimum energy. The numerical values of the parameters  $a_{11}$  to  $a_{16}$  were determined from the least-squares fitting of the Monte Carlo-obtained spectra, using the primary and secondary spectra calculated using Eqs. (1) and (4), respectively. The results of the fitting are also summarized in Table 1.

The PARMA results for proton and helium-ion spectra shown in Figs. 2 and 4 were obtained by substituting all the parameters and equations given in this section into Eq. (11). The figures clearly indicate the ability of PARMA to reproduce the Monte Carlo simulation results except for the proton spectra below 10 MeV and the helium-ion spectra at intermediate energies, around 100 MeV/nucleon. The disagreement in the helium-ion spectra is attributed to the fact that helium ions with such an intermediate energy were generally produced by the pre-equilibrium or nuclear fragmentation processes, but we assumed that all secondary he-

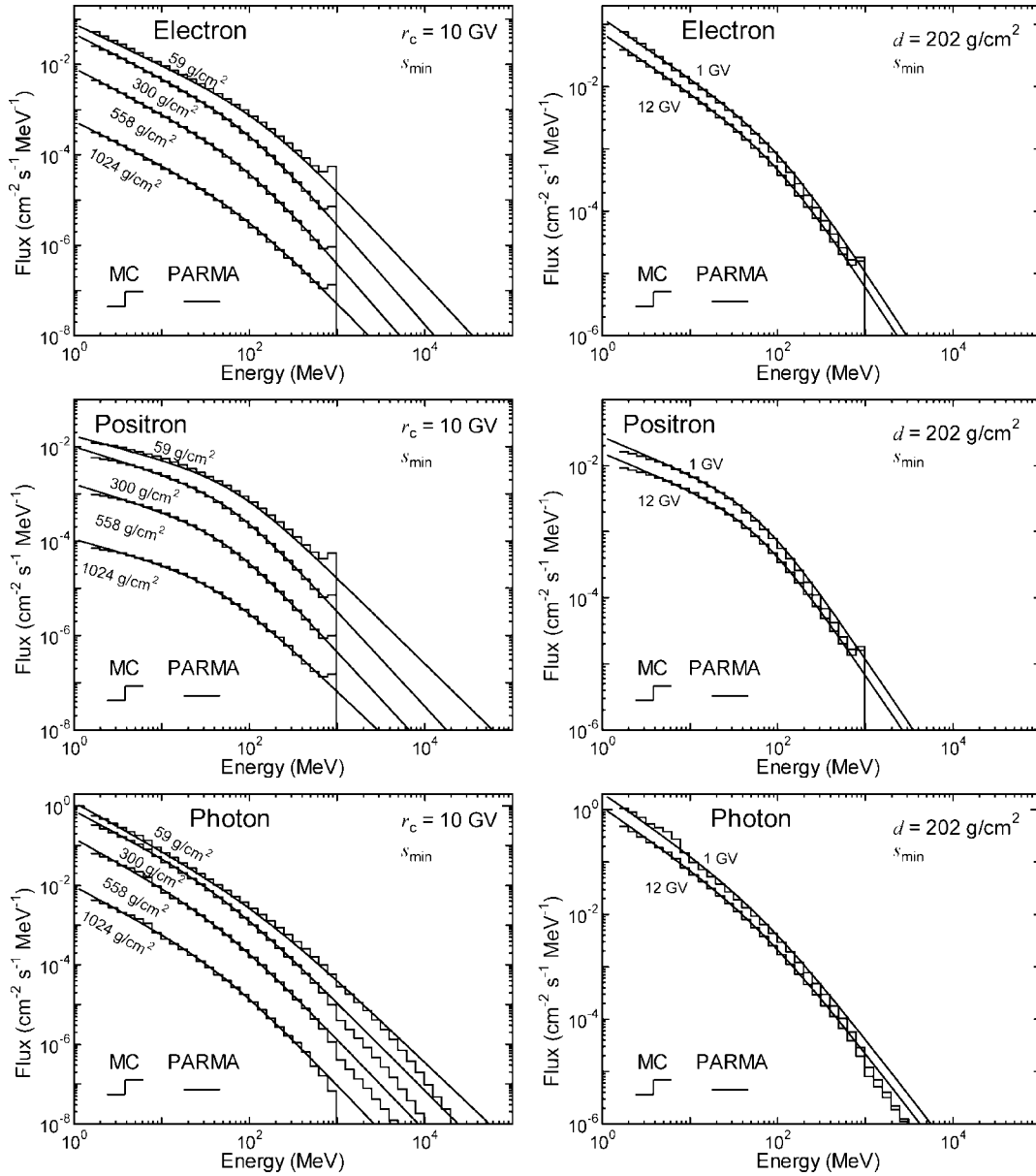


**FIG. 7.** Comparison between the cosmic-ray electron, positron and photon spectra obtained by our Monte Carlo simulation and PARMA. The left and right panels show the atmospheric depth and the cut-off rigidity dependence of the spectra, respectively.

limum ions were created by the evaporation process in the derivation of PARMA. However, the doses from protons below 10 MeV and helium ions between 20 MeV/nucleon and 1 GeV/nucleon are less than 1% of their total values in most cases. Hence the effects of these discrepancies on the dose estimation can be considered to be negligible.

#### *Electron, Positron and Photon Spectra*

Figure 7 shows the cosmic-ray electron, positron and photon spectra obtained by the Monte Carlo simulation, together with the corresponding data calculated by PARMA. In the simulation, all electrons, positrons and photons were generated in the Earth system, i.e. were second-

ary particles, since only protons and heavy ions were considered to be source particles incident to the atmosphere. We therefore assumed that the electron, positron and photon spectra can be estimated in a manner similar to the secondary proton spectra described before. The difference between the calculation procedures for secondary proton spectra and the others is that we normalized the electron, positron and photon spectra to their fluxes at 10 MeV instead of those at 1 MeV. This is because the photon fluxes below a few MeV are influenced by the cut-off rigidity and thus are inadequate for use in the normalization of the spectra. The parameters  $c_{ij}$  and  $h_{ij}$  used in Eqs. (5) and (7), respectively, for estimating the atmospheric electron, posi-

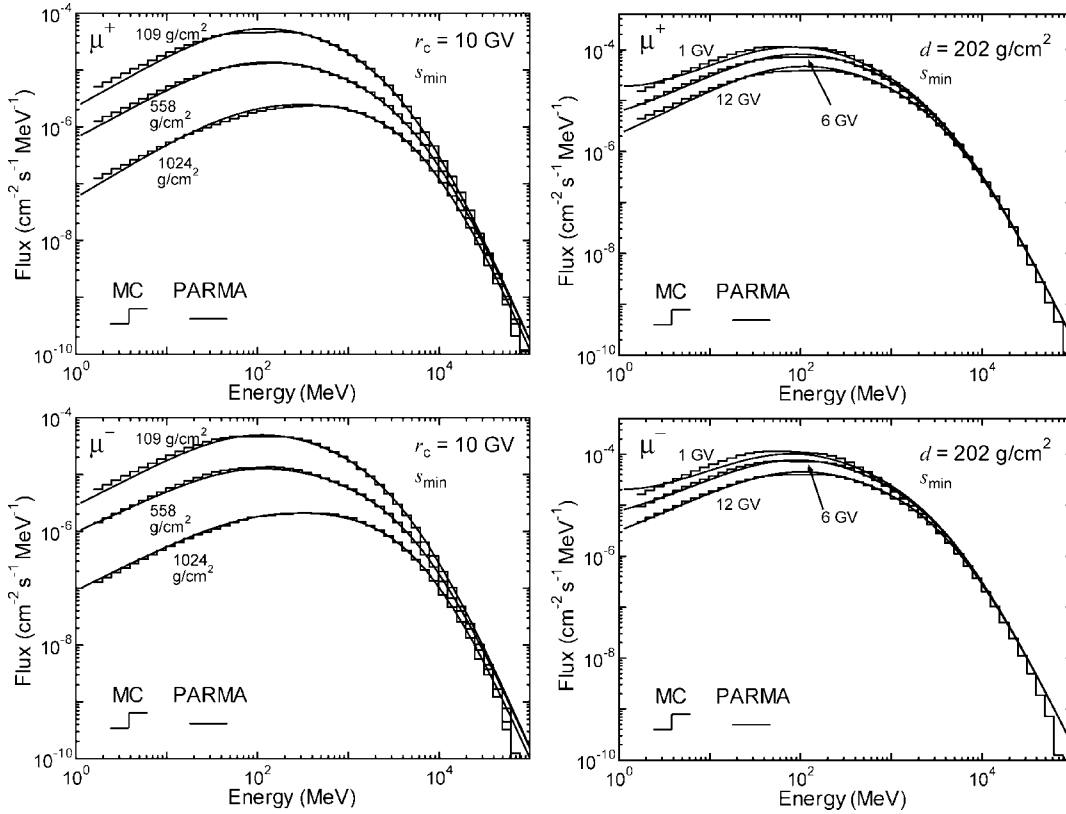


**FIG. 8.** Comparison between the cosmic-ray muon spectra obtained by our Monte Carlo simulation and PARMA. The left and right panels show the atmospheric depth and the cut-off rigidity dependence of the spectra, respectively.

tron and photon spectra are also listed in Tables 2 and 3, where their numerical values were determined from the least-squares fittings of the corresponding Monte Carlo data.

The PARMA results for electron, positron and photon spectra shown in Figs. 2 and 7 were obtained by substituting the results of Eqs. (5) and (8) into Eq. (4), using parameters listed in Tables 2 and 3. It is evident from the graphs that PARMA can reproduce the corresponding Monte Carlo data for energies below 1 GeV. Above 1 GeV, on the other hand, the analytical fluxes obtained for photons as well as electrons and positrons are generally larger than the Monte Carlo data. Thus their doses estimated by PARMA are approximately 10% higher than those obtained by the Monte Carlo simulation. However, this disagreement is not directly connected to a decrease in the reliability of PARMA with respect to the aircrew dose estimation, since their spectra in the high-energy region obtained by the Monte Carlo simulation are supposed to be underestimated for two reasons: (1) High-energy electrons and positrons were not transported, and (2) incident cosmic rays with energy above 200 GeV/nucleon, which can produce a large number of high-energy photons, electrons and positrons, were not considered in our simulation.

#### Muon Spectra

Figure 8 shows the dependence of muon spectra on the atmospheric depth and the cut-off rigidity. Although all of

the cosmic-ray muons are secondary particles, as are the electrons, positrons and photons, the muon spectra cannot be estimated by the same procedure, i.e. normalizing their spectra to their flux at a certain energy. This is because the atmospheric depth dependence of the muon fluxes even at lower energies cannot be expressed by Eq. (6) because the strong penetrability of muons prevents equilibrium between the numbers of incoming and outgoing particles. We therefore constructed the model for predicting atmospheric muon spectra based on that for estimating underground muon spectra proposed by Lipari *et al.* (36).

According to their model, underground muon spectra  $dN/dE$  can be expressed by

$$\frac{dN}{dE} = \alpha_1 \exp[(1 - \alpha_3)\alpha_2 X] \times \left\{ E + \frac{\alpha_4 X}{\alpha_2 X} [1 - \exp(-\alpha_2 X)] \right\}^{-\alpha_3}, \quad (14)$$

where  $X$  denotes the depth of rock and  $\alpha_i$  are constants. Note that the notations of some parameters are changed from the original equation to avoid the duplicate use of a notation in this paper. For the boundary condition, they assumed that the muon spectrum at the ground level can be expressed as  $\alpha_1 E^{-\alpha_3}$ , where  $\alpha_3 = 3.7$ , close to the spectrum expected for muons generated by pion and kaon decays in the atmosphere. The parameters  $\alpha_2$  and  $\alpha_4$  are re-

lated to the radiation and ionization energy loss of high-energy muons, respectively, and their stopping power can be written as  $\alpha_2 E + \alpha_4$ .

This equation, however, cannot be applied directly to the estimation of the atmospheric muon spectra, since not only deceleration but also production and decay of muons must be considered in their calculation. To take the production into account,  $\alpha_1$  should be replaced by functions that depend on the atmospheric depth in a complicated manner. Furthermore, the assumption that  $\alpha_4$  is a constant is inadequate for our purpose, since it depends significantly on  $\beta$  at lower energies and increases slightly with a logarithmic increase of muon energy at higher energies, as expected from the Bethe-Bloch formula. On the other hand,  $\alpha_2 X$  is expected to be very small for atmospheric muons, since the track length of a muon in the atmosphere is at most  $10^3$  g/cm<sup>2</sup>, which is much shorter than  $1/\alpha_2$ . Consequently, the approximations of  $\exp[(1 - \alpha_3)\alpha_2 X] \sim 1$  and  $[1 - \exp(-\alpha_2 X)] \sim \alpha_2 X$  are established.

From these considerations, we proposed a best-fit curve to the atmospheric muon fluxes for the solar minimum condition,  $\Phi_{\mu\text{min}}$ , as generated by the equation

$$\begin{aligned} \Phi_{\mu\text{min}}(r_c, d, E) \\ = \Phi_{\mu}(d) \left[ E + \frac{t_{1\text{min}}(r_c, d) + t_{2\text{min}}(r_c, d) \log_{10}(E)}{\beta^{t_{3\text{min}}(r_c, d)}} \right]^{-\alpha_3}, \end{aligned} \quad (15)$$

where  $\Phi_{\mu}$  is an index for the high-energy muon fluxes at the atmospheric depth  $d$ , and  $t_i$  are parameters related to the mean ionization energy loss of muons during the transport through the atmosphere. Note that  $\Phi_{\mu}$  depends only on the atmospheric depth, since the high-energy muon fluxes are independent of the solar modulation and the cut-off rigidity. In the derivation of this equation, we assumed that the mean energy loss due to the ionization can be expressed by a linear function of the common logarithm of  $E$  divided by a power function of  $\beta$ , since it depends on the global condition in a complicated manner and cannot be calculated directly by theoretical formulas such as the Bethe-Bloch formula. The muon fluxes for the solar maximum condition,  $\Phi_{\mu\text{max}}$ , can be also estimated from Eq. (15) by replacing the subscript “min” with “max” in the equation.

For a best-fit curve to  $\Phi_{\mu}$ , we introduced a function with the form similar to Eq. (6) as written by

$$\Phi_{\mu}(d) = u_1[\exp(-u_2 d) - u_3 \exp(-u_4 d)] + u_5, \quad (16)$$

where  $u_i$  are free parameters. For that to  $t_i$ , we simply adopted the fourth order of the polynomial function:

$$\begin{aligned} t_i(r_c, d) = v_{i1}(r_c) + v_{i2}(r_c)d + v_{i3}(r_c)d^2 \\ + v_{i4}(r_c)d^3 + v_{i5}(r_c)d^4, \end{aligned} \quad (17)$$

where  $v_{ij}$  are parameters related to the solar modulation and the cut-off rigidity. For expressing the dependence of  $v_{ij}$  on

$r_c$ , we employed a function with the same form as Eq. (7) as written by

$$v_{ij}(r_c) = w_{ij1} + w_{ij2}r_c + \frac{w_{ij3}}{1 + \exp[(r_c - w_{ij4})/w_{ij5}]}, \quad (18)$$

where  $w_{ijk}$  are free parameters. The parameters  $v_{ij}$  for  $r_c < 1$  GV are regarded as the constant values of those at  $r_c = 1$  GV, as described before. The numerical values of the parameters  $u_i$  together with  $w_{ijk}$  for the solar minimum and maximum conditions were determined from the least-squares fitting of the Monte Carlo-obtained  $\Phi_{\mu}$  data for the force field potentials 400 and 1200 MV, respectively. In the fitting, the numerical value of  $\alpha_3$  is fixed at 3.7, following the original Lipari model. The atmospheric muon spectra for arbitrary solar conditions can be estimated from  $\Phi_{\mu\text{min}}$  and  $\Phi_{\mu\text{max}}$  calculated by Eq. (15), assuming that  $\Phi_{\mu}$  depends on the force field potential in the same manner of  $\Phi_N$  as written by Eq. (8). For muons, the numerical values of the parameters  $h_{5j}$  and  $h_{6j}$  in Eq. (7) for determining  $g_5$  and  $g_6$  in Eq. (9) were obtained from the least-squares fitting of the Monte Carlo-obtained energy-integrated  $\Phi_{\mu}$  for all force field potentials—400, 600, 900, 1200 and 1800 MV. The results of these least-squares fittings are summarized in Table 4.

The PARMA results for muon spectra shown in Figs. 2 and 8 were calculated by substituting the evaluated  $u_i$  in this section into Eq. (15). It is evident from the graphs that the PARMA results closely agree with the Monte Carlo data except for energies below 10 MeV and above 20 GeV. The discrepancy in the low-energy region is not important in the dose estimation, since doses from such low-energy muons are negligibly small—much less than 1% of their total values. That in the high-energy region is attributed to the fact that such high-energy muons are generally produced by nuclear reactions caused by cosmic rays with energies above 200 GeV, which are not considered in the Monte Carlo simulation. According to theory, the high-energy muon spectra can be simply expressed by a power function of the muon energy, and hence the PARMA results are more reliable than the corresponding Monte Carlo data in the high-energy region. This tendency is also verified by the comparison of the Monte Carlo-obtained and experimental muon spectra shown in Fig. 3C and D, where the Monte Carlo simulation underestimates the experimental data in the high-energy region.

#### Comparison with Monte Carlo Simulation in Terms of Dose Estimation

To verify the agreement between PARMA and the Monte Carlo simulation in dose estimation, the ratios of the doses calculated by PARMA to those by the Monte Carlo simulation were evaluated for 1620 global conditions: five force field potentials from 400 to 1800 MV, 18 geomagnetic fields with vertical cut-off rigidities from 0 to 17 GV, and 18 altitude ranges from sea level to 20 km. In the dose

**TABLE 4**  
**Numerical Values of the Parameters  $u_i$ ,  $w_{ijk}$  and  $h_j$  used in Eqs. (16), (18) and (7), respectively, to Estimate the Atmospheric Muon Spectra**

Parameter	$\mu^+$				
	$u_1$	$u_2$	$u_3$	$u_4$	$u_5$
$\Phi_\mu$	$6.26 \times 10^9$	0.00343	1.01	0.00418	$3.75 \times 10^8$
Parameter	$w_{i1}$	$w_{i2}$ (GV <sup>-1</sup> )	$w_{i3}$	$w_{i4}$ (GV)	$w_{i5}$ (GV)
$v_{11\min}$	$2.05 \times 10^3$	126	$-1.01 \times 10^3$	6.18	3.47
$v_{11\max}$	$2.39 \times 10^3$	118	-949	7.04	3.84
$v_{12\min}$	-5.67	-0.655	3.59	1.31	3.22
$v_{12\max}$	-5.62	-0.658	3.28	1.06	3.34
$v_{13\min}$	0.0117	0.00157	-0.0125	3.26	3.65
$v_{13\max}$	0.0117	0.00157	-0.0124	3.31	3.58
$v_{14\min}$	$-2.31 \times 10^{-6}$	$-7.60 \times 10^{-7}$	$2.48 \times 10^{-5}$	4.94	3.80
$v_{14\max}$	$-2.24 \times 10^{-6}$	$-7.56 \times 10^{-7}$	$2.48 \times 10^{-5}$	4.89	3.80
$v_{15\min}$	$1.74 \times 10^{-9}$	$-2.22 \times 10^{-10}$	$-1.69 \times 10^{-8}$	5.12	4.39
$v_{15\max}$	$1.75 \times 10^{-9}$	$-2.26 \times 10^{-10}$	$-1.69 \times 10^{-8}$	5.18	4.40
$v_{21\min}$	84.8	-5.77	370	4.81	3.36
$v_{21\max}$	87.3	-5.90	377	4.59	3.39
$v_{22\min}$	3.41	0.0787	-0.520	6.87	1.09
$v_{22\max}$	3.41	0.0785	-0.523	6.84	1.09
$v_{23\min}$	-0.00332	$-1.49 \times 10^{-4}$	0.00185	7.02	0.607
$v_{23\max}$	-0.00331	$-1.49 \times 10^{-4}$	0.00185	7.02	0.611
$v_{24\min}$	$-2.68 \times 10^{-6}$	$-8.88 \times 10^{-8}$	$-2.71 \times 10^{-6}$	7.04	0.4685
$v_{24\max}$	$-2.68 \times 10^{-6}$	$-8.81 \times 10^{-8}$	$-2.71 \times 10^{-6}$	7.04	0.472
$v_{25\min}$	$2.33 \times 10^{-9}$	$1.49 \times 10^{-10}$	$1.20 \times 10^{-9}$	7.04	0.364
$v_{25\max}$	$2.32 \times 10^{-9}$	$1.49 \times 10^{-10}$	$1.20 \times 10^{-9}$	7.05	0.367
$v_{31\min}$	0.760	-0.0180	-0.273	11.3	5.39
$v_{31\max}$	0.923	-0.0296	-0.428	9.66	4.00
$v_{32\min}$	0.00206	$6.17 \times 10^{-5}$	0.00178	7.55	3.93
$v_{32\max}$	$8.44 \times 10^{-4}$	$1.34 \times 10^{-4}$	0.00181	9.26	2.44
$v_{33\min}$	$-5.96 \times 10^{-6}$	$-1.48 \times 10^{-7}$	$-4.13 \times 10^{-6}$	7.53	4.39
$v_{33\max}$	$-3.91 \times 10^{-6}$	$-2.88 \times 10^{-7}$	$-2.49 \times 10^{-6}$	9.74	1.49
$v_{34\min}$	$6.46 \times 10^{-9}$	$-9.28 \times 10^{-12}$	$1.74 \times 10^{-9}$	23.6	1.67
$v_{34\max}$	$1.99 \times 10^{-9}$	$3.57 \times 10^{-10}$	$2.95 \times 10^{-9}$	10.4	1.94
$v_{35\min}$	$-3.21 \times 10^{-12}$	$5.46 \times 10^{-14}$	$9.21 \times 10^{-13}$	7.54	2.66
$v_{35\max}$	$-1.78 \times 10^{-12}$	$-3.17 \times 10^{-14}$	$4.79 \times 10^{-13}$	4.21	0.747
Parameter	$h_{i1}$	$h_{i2}$ (GV <sup>-1</sup> )	$h_{i3}$	$h_{i4}$ (GV)	$h_{i5}$ (GV)
$g_5$	0.506	0.0130	-0.394	4.12	1.33
$g_6$ (cm <sup>2</sup> g <sup>-1</sup> )	$1.39 \times 10^{-4}$	$6.95 \times 10^{-6}$	$7.47 \times 10^{-4}$	3.72	1.97

calculation, we adopted the fluence to effective dose conversion coefficients for the isotropic irradiation geometry calculated by PHITS (37, 38) coupled with the updated radiation weighting factor defined in ICRP publication 103 (39). It should be noted that the Monte Carlo simulation took more than 1 month using a parallel computer with 24 CPUs, while the dose calculation by PARMA took only 10 s using a conventional PC. This difference clearly indicates the efficiency of PARMA when it is adopted in the route-dose calculation.

Figure 9 shows the distributions of the ratios of the doses calculated by PARMA to those obtained from the Monte Carlo simulation for each particle type as well as that for the total dose. It should be noted that the total doses obtained by the Monte Carlo simulation include the doses from particles whose spectrum model was not developed in this paper, i.e. pions and heavy ions with  $Z \geq 3$ , but their contributions are generally negligible—less than 1% of the total. It is evident from this graph that the total doses cal-

culated by PARMA and the Monte Carlo simulation agree with each other within 5% for more than 99% of the global conditions, indicating the equivalence of the PARMA and the Monte Carlo simulation with respect to the accuracy of dose estimation. The distribution of this ratio for helium ions is broad in comparison to those for other particles, but most of the scattered data are for lower altitudes, where the contribution of helium ions to the total dose is negligible. The ratios for electrons, positrons and photons are generally greater than 1 by approximately 10%, since PARMA gives higher values for these fluxes above 1 GeV than to the Monte Carlo simulation, as described before.

## CONCLUSIONS

Monte Carlo simulations were performed for estimating cosmic-ray spectra in the atmosphere using the PHITS code. Excellent agreement was observed between the calculated and measured spectra for various conditions, except

**TABLE 4**  
**Extended**

$\mu^-$				
$u_1$	$u_2$	$u_3$	$u_4$	$u_5$
$5.82 \times 10^9$	0.00362	1.02	0.00451	$3.20 \times 10^8$
$w_{ij1}$	$w_{ij2}$ (GV <sup>-1</sup> )	$w_{ij3}$	$w_{ij4}$ (GV)	$w_{ij5}$ (GV)
$2.09 \times 10^3$	121	-929	6.86	3.29
$2.42 \times 10^3$	112	-895	7.45	3.55
-5.66	-0.650	3.58	0.89	3.73
-5.61	-0.651	3.31	0.78	3.76
0.0118	0.00158	-0.0125	3.44	3.65
0.0118	0.00158	-0.0125	3.48	3.59
$-2.59 \times 10^{-6}$	$-7.99 \times 10^{-7}$	$2.54 \times 10^{-5}$	4.95	3.72
$-2.52 \times 10^{-6}$	$-7.93 \times 10^{-7}$	$2.53 \times 10^{-5}$	4.92	3.74
$1.87 \times 10^{-9}$	$-1.98 \times 10^{-10}$	$-1.71 \times 10^{-8}$	5.12	4.24
$1.86 \times 10^{-9}$	$-2.01 \times 10^{-10}$	$-1.70 \times 10^{-8}$	5.14	4.27
85.9	-5.86	369	4.82	3.30
87.0	-5.88	372	4.68	3.30
3.42	0.0790	-0.529	6.88	1.06
3.42	0.0787	-0.532	6.86	1.09
$-3.33 \times 10^{-3}$	$-1.49 \times 10^{-4}$	0.00186	7.04	0.602
$-3.32 \times 10^{-3}$	$-1.50 \times 10^{-4}$	0.00186	7.04	0.601
$-2.69 \times 10^{-6}$	$-9.00 \times 10^{-8}$	$-2.71 \times 10^{-6}$	7.05	0.464
$-2.68 \times 10^{-6}$	$-8.93 \times 10^{-8}$	$-2.71 \times 10^{-6}$	7.05	0.465
$2.34 \times 10^{-9}$	$1.50 \times 10^{-10}$	$1.19 \times 10^{-9}$	7.05	0.356
$2.33 \times 10^{-9}$	$1.50 \times 10^{-10}$	$1.20 \times 10^{-9}$	7.04	0.362
0.787	-0.0180	-0.304	14.5	5.61
0.814	-0.0248	-0.311	10.6	3.61
0.00214	$4.99 \times 10^{-5}$	0.00143	8.10	3.46
$6.65 \times 10^{-4}$	$1.35 \times 10^{-4}$	0.00184	9.29	2.39
$-6.05 \times 10^{-6}$	$-1.36 \times 10^{-7}$	$-3.94 \times 10^{-6}$	7.83	4.34
$-3.80 \times 10^{-6}$	$-2.92 \times 10^{-7}$	$-2.58 \times 10^{-6}$	9.67	1.38
$6.68 \times 10^{-9}$	$1.09 \times 10^{-12}$	$1.58 \times 10^{-9}$	22.7	1.99
$2.75 \times 10^{-9}$	$3.35 \times 10^{-10}$	$2.31 \times 10^{-9}$	10.3	1.37
$-3.10 \times 10^{-12}$	$3.80 \times 10^{-14}$	$7.46 \times 10^{-13}$	7.85	2.00
$-1.81 \times 10^{-12}$	$-4.17 \times 10^{-14}$	$4.63 \times 10^{-13}$	4.54	0.479
$h_{i1}$	$h_{i2}$ (GV <sup>-1</sup> )	$h_{i3}$	$h_{i4}$ (GV)	$h_{i5}$ (GV)
0.565	0.0121	-0.357	4.73	1.46
$8.80 \times 10^{-5}$	$-3.89 \times 10^{-6}$	$4.91 \times 10^{-4}$	4.51	1.72

for the electron data. Further study is needed to improve the accuracy of the PHITS simulation in regard to electron and positron transport, since the cosmic-ray electron spectra obtained by the simulation do not agree well with some experimental data due to the uncertain calculation technique for dealing with the transport of high-energy electrons and positrons in the code. Based on a comprehensive analysis of the simulation results, we proposed an analytical model for estimating the atmospheric cosmic-ray spectra for neutrons, protons, helium ions, muons, electrons, positrons and photons that is applicable to any global conditions at altitudes below 20 km. The PARMA model enables us to calculate the cosmic-radiation doses instantaneously with precision equivalent to that of the Monte Carlo simulation that requires much computational time, although some discrepancies are observed between their calculated spectra for certain particle types and energies. One shortcoming of PARMA is that it adopts the vertical cut-off rigidity instead of its full two-dimensional distribution in the consideration

of the magnetosphere on the cosmic-ray spectra, but the resulting errors are expected to be small except for the magnetic equator region, as discussed in ref. (5). We therefore conclude that PARMA can improve the accuracy and efficiency of cosmic-ray exposure dose estimations not only for aircrews but also for the public on the ground.

For the practical use of PARMA, software based on the model that we named EXPACS was developed for calculating atmospheric cosmic-ray spectra. It has been released to the public online (40). In the near future, PARMA will be incorporated into the Japanese Internet System for Calculation of Aviation Route Doses (JISCARD) (41) and used for adhering to the dose limit (<5 mSv/year) recommended for aircrews of Japanese airline companies. The accuracy of the updated JISCARD is currently being evaluated by comparing its calculated route doses with the corresponding experimental data under various flight conditions, and the results will be presented in our forthcoming paper. The simulation technique established by this work is also capable

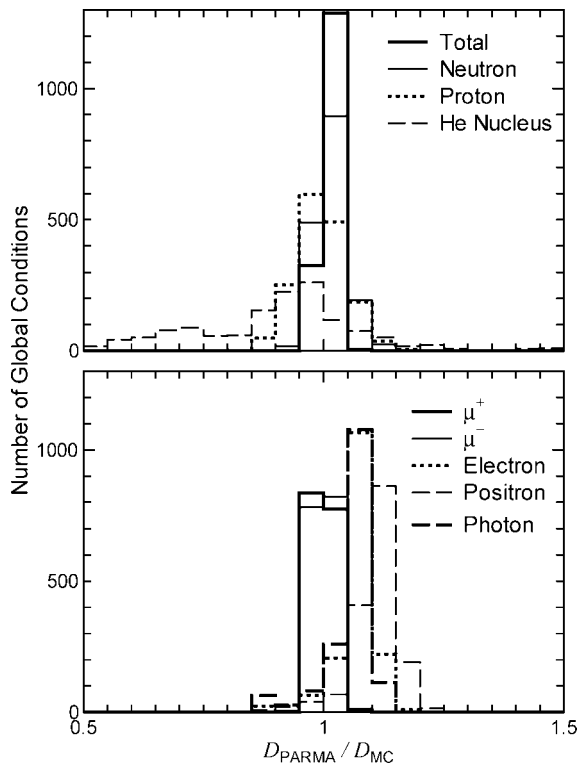


FIG. 9. Distributions of the ratios of doses calculated by PARMA to those obtained by our Monte Carlo simulation.

of contributing to the estimation of the atmospheric cosmic-ray spectra under solar-geomagnetic storm conditions, an area requiring additional study. Application of this work to the estimation of cosmic-ray spectra on the Martian surface will be of great interest in future NASA human space explorations.

#### ACKNOWLEDGMENTS

We would like to thank Dr. Y. Watanabe and Dr. T. Fukahori for their support in incorporating JENDL/HE into PHITS, Dr. M. Honda and Dr. K. O'Brien for their advice on constructing the model for estimating the cosmic-ray spectra at the top of the atmosphere, and Dr. T. Nakamura for his valuable comments on this work. We also wish to thank the technical staff of the CCSE office of JAEA for their help in performing the Monte Carlo simulation. This work was partially supported by "Ground-based Research Program for Space Utilization" promoted by the Japan Space Forum.

Received: May 18, 2007; accepted: March 24, 2008

#### REFERENCES

1. ICRP, *1990 Recommendations of the International Commission on Radiological Protection*. Publication 60, *Annals of the ICRP*, Vol. 21, No. 1–3, Pergamon Press, Oxford, 1991.
2. H. Schraube, V. Mares, S. Roesler and W. Heinrich, Experimental verification and calculation of aviation route doses. *Radiat. Prot. Dosimetry* **86**, 309–315 (1999).
3. W. Friedberg, K. Copeland, F. E. Duke, K. O'Brien and E. B. Darden, Guidelines and technical information provided by the U.S. Federal Aviation Administration to promote radiation safety for air carrier crew members. *Radiat. Prot. Dosimetry* **86**, 323–327 (1999).

4. B. J. Lewis, L. G. I. Bennett, A. R. Green, A. Butler, M. Desormeaux, F. Kitching, M. J. McCall, B. Ellaschuk and M. Pierre, Aircrew dosimetry using the predictive code for aircrew radiation exposure (PCAIRE). *Radiat. Prot. Dosimetry* **116**, 320–326 (2005).
5. K. O'Brien, W. Friedberg, H. H. Sauer and D. F. Smart, Atmospheric cosmic rays and solar energetic particles at aircraft altitudes. *Environ. Int.* **22** (Suppl. 1), S9–S44 (1996).
6. D. Heck, J. Knapp, J. N. Capdevielle, G. Schatz and T. Thouw, *CORSIKA: A Monte Carlo Code to Simulate Extensive Air Showers*. Report FZKA 6019, Forschungszentrum Karlsruhe, 1998. <http://www.ik.fzk.de/corsika/>.
7. COSMOS: A versatile Monte Carlo simulation code for propagation of cosmic rays in the atmosphere and near earth environment. <http://cosmos.n.kanagawa-u.ac.jp/cosmosHome/index.html>.
8. PLANETOCOSMICS GEANT4. <http://cosray.unibe.ch/~laurent/planetocosmics/>.
9. A. Fasso, A. Ferrari and P. R. Sala, Electron-photon transport in FLUKA: status. In *Proceedings of the Monte Carlo 2000 Conference*, Lisbon, Oct. 23–26 (A. Kling, F. Barao, M. Nakagawa, L. Tavora and P. Vaz, Eds.), pp. 159–164. Springer-Verlag, Berlin, 2001.
10. A. Fasso, A. Ferrari, J. Ranft and P. R. Sala, FLUKA: status and prospective for hadronic applications. In *Proceedings of the Monte Carlo 2000 Conference*, Lisbon, Oct. 23–26 (A. Kling, F. Barao, M. Nakagawa, L. Tavora, P. Vaz, Eds.), pp. 955–960. Springer-Verlag, Berlin, 2001.
11. J. M. Clem, G. De Angelis, P. Goldhagen and J. W. Wilson, New calculations of the atmospheric cosmic radiation field—results for neutron spectra. *Radiat. Prot. Dosimetry* **110**, 423–428 (2004).
12. H. Iwase, K. Niita and T. Nakamura, Development of a general-purpose particle and heavy ion transport Monte Carlo code. *J. Nucl. Sci. Technol.* **39**, 1142–1151 (2002).
13. T. Fukahori, Y. Watanabe, N. Yoshizawa, F. Maekawa, S. Meigo, C. Konno, N. Yamano, A. Yu. Konobeyev and S. Chiba, JENDL High Energy File. *J. Nucl. Sci. Technol.* (Suppl. 2), 25–30 (2002).
14. Y. Watanabe, T. Fukahori, K. Kosako, N. Shigyo, T. Murata, N. Yamano, T. Hino, K. Maki, H. Nakashima, N. Odano and S. Chiba, Nuclear data evaluations for JENDL high-energy file. In *Proceedings of International Conference on Nuclear Data for Science and Technology*, pp. 326–331. AIP CP769, American Institute of Physics, Melville, NY, 2005.
15. T. Sato and K. Niita, Analytical functions to predict cosmic-ray neutron spectra in the atmosphere. *Radiat. Res.* **166**, 544–555 (2006).
16. K. O'Brien, H. A. Sandmeier, G. E. Hansen and J. E. Campbell, Cosmic-ray-induced neutron background sources and fluxes for geometries of air over water, ground, iron, and aluminum. *J. Geophys. Res.* **83**, 114–120 (1978).
17. S. Roesler, W. Heinrich and H. Schraube, Calculation of radiation fields in the atmosphere and comparison to experimental data. *Radiat. Res.* **149**, 87–97 (1998).
18. R. A. Nymmik, M. I. Panasyuk, T. I. Pervaja and A. A. Suslov, A model of galactic cosmic ray fluxes. *Nucl. Tracks Radiat. Meas.* **20**, 427–429 (1992).
19. L. J. Gleeson and W. I. Axford, Modulation of galactic cosmic rays. *Astrophys. J.* **154**, 1011–1026 (1968).
20. R. A. Caballero-Lopez and H. Moraal, Limitations of the force field equation to describe cosmic ray modulation. *J. Geophys. Res.* **109**, A01101 (2004).
21. K. O'Brien, E. Felsberger and P. Kindl, Application of the heliocentric potential to aircraft dosimetry. *Radiat. Prot. Dosimetry* **116**, 336–342 (2005).
22. Y. Shikaze, S. Haino, K. Abe, H. Fuke, T. Hams, K. C. Kim, Y. Makida, S. Matsuda, J. W. Mitchell and K. Yoshimura, Measurements of 0.2–20 GeV/n cosmic-ray proton and helium spectra from 1997 through 2002 with the BESS spectrometer. *Astropart. Phys.* **28**, 154–167 (2007).
23. Index to /ftp/pub/WDCCR. <http://www.env.sci.ibaraki.ac.jp/ftp/pub/WDCCR>.

24. H. W. Bertini, Low-energy intranuclear cascade calculation. *Phys. Rev.* **131**, 1801–1821 (1963).
25. P. Goldhagen, J. M. Clem and J. W. Wilson, The energy spectrum of cosmic-ray induced neutrons measured on an airplane over a wide range of altitude and latitude. *Radiat. Prot. Dosimetry* **110**, 387–392 (2004).
26. N. M. Kocharian, G. S. Saakian and Z. A. Kirakosian, Energy spectra and nuclear interactions of cosmic-ray particles. *Sov. Phys. JETP* **35**, 933–942 (1959).
27. I. S. Diggory, J. R. Hook, I. A. Jenkins and K. E. Turver, The momentum spectra of nuclear active particles in the cosmic radiation at sea level I. Experimental data. *J. Phys. A Math. Nucl. Gen.* **7**, 741–764 (1974).
28. H. B. Barber, T. Bowen, D. A. Delise, E. W. Jenkins, J. J. Jones, R. M. Kalbach and A. E. Pifer, Predictions and measurements of mass spectra of the charged nucleonic component of cosmic rays at mountain altitude. *Phys. Rev.* **22**, 2667–2687 (1980).
29. T. Sanuki, M. Fujikawa, H. Matsunaga, K. Abe, K. Anraku, H. Fuke, S. Haino, M. Imori, K. Izumi and K. Yoshimura, Measurement of cosmic-ray proton and antiproton spectra at mountain altitude. *Phys. Lett.* **577**, 10–17 (2003).
30. J. Kremer, M. Boezio, M. L. Ambriola, G. Barbiellini, S. Bartalucci, R. Bellotti, D. Bergstrom, U. Bravar, F. Cafagna and N. Zamp, Measurements of ground-level muons at two geomagnetic locations. *Phys. Rev. Lett.* **83**, 4241–4244 (1999).
31. T. Sanuki, M. Fujikawa, K. Abe, K. Anraku, Y. Asaoka, H. Fuke, S. Haino, M. Imori, K. Izumi and K. Yoshimura, Measurement of atmospheric muon spectra at mountain altitude. *Phys. Lett. B* **541**, 234–242 (2002).
32. S. Haino, T. Sanuki, K. Abe, K. Anraku, Y. Asaoka, H. Fuke, M. Imori, A. Itasaki, T. Maeno and K. Yoshimura, Measurements of primary and atmospheric cosmic-ray spectra with the BESS-TeV spectrometer. *Phys. Lett. B* **594**, 35–46 (2004).
33. S. Cecchini, T. Chiarusi, A. Pagliarin and G. Giovannini, On the altitude dependence of  $\gamma$ -rays spectra in the Earth's atmosphere. In *Proceedings of 29th International Cosmic Ray Conference*, Vol. 2, pp. 349–352. Pune, India, 2005.
34. G. J. Fulks and P. Meyer, Cosmic ray electrons in the atmosphere. *J. Geophys.* **40**, 751–759 (1974).
35. M. Honda, T. Kajita, K. Kasahara, S. Midorikawa, T. Sanuki, J. Nishimura and A. Okada, Reducing uncertainty in atmospheric neutrino flux prediction. In *Proceedings of 30th International Cosmic Ray Conference*, 0274. Merida, Mexico, 2007.
36. P. Lipari and T. Stanev, Propagation of multi-TeV muons. *Phys. Rev. D* **44**, 3543–3554 (1991).
37. T. Sato, S. Tsuda, Y. Sakamoto, Y. Yamaguchi and K. Niita, Conversion coefficients from fluence to effective dose for heavy ions with energies up to 3 GeV/A. *Radiat. Prot. Dosimetry* **106**, 137–144 (2003).
38. T. Sato, S. Tsuda, Y. Sakamoto, Y. Yamaguchi and K. Niita, Analysis of dose-LET distribution in the human body irradiated by high energy hadrons. *Radiat. Prot. Dosimetry* **106**, 145–153 (2003).
39. ICRP, *The 2007 Recommendations of the International Commission on Radiological Protection*. ICRP Publication 103, *Annals of the ICRP*, Vol. 37, No. 2–4, Elsevier, Oxford, 2007.
40. EXPACS, Excel-based Program for Calculating Atmospheric Cosmic-ray Spectrum. <http://www.jaea.go.jp/04/nsed/ers/radiation/rpro/EXPACS/expacs-eng.html>.
41. JISCARD, Japanese Internet System for Calculation of Aviation Route Doses. <http://www.nirs.go.jp/research/jiscard/information/index.shtml>. [in Japanese]